

# Mapping LiDAR and Camera Measurements in a Dual Top-View Grid Representation Tailored for Automated Vehicles

Sven Richter<sup>1,\*</sup>, Frank Bieder<sup>1,2</sup>, Sascha Wirges<sup>3</sup> and Christoph Stiller<sup>1,2</sup>

**Abstract**—We present a generic evidential grid mapping pipeline designed for imaging sensors such as LiDAR and cameras. Our grid-based evidential model contains semantic estimates for cell occupancy and ground separately. We specify the estimation steps for input data represented by point sets, but mainly focus on input data represented by images such as disparity maps or LiDAR range images. Instead of relying on an external ground segmentation only, we deduce occupancy evidence by analyzing the surface orientation around measurements. We conduct experiments and evaluate the presented method using LiDAR and stereo camera data recorded in real traffic scenarios. Our method estimates cell occupancy robustly and with a high level of detail while maximizing efficiency and minimizing the dependency to external processing modules.

**Index Terms**—Autonomous driving, environment perception, evidential grid maps, semantic segmentation, LiDAR, camera.

## I. INTRODUCTION

Traffic scene perception is one of the key tasks in the development of software components for automated transportation systems. Imaging sensors such as light detection and ranging (LiDAR) and cameras play an important role in this context. LiDARs measure the distance to reflecting surfaces and thus enable the detection of obstacles and free space. In contrast to LiDARs, cameras do not measure the distance to reflecting surfaces directly. Instead, depth estimates must be provided based on the sensor readings by utilizing Computer Vision algorithms. Stereo cameras enable the deduction of range estimates by finding corresponding pixels using epipolar geometry and calculated disparity values, see e.g. [1], [2]. The pixel disparities are then used to infer three-dimensional (3D) pixel coordinates. In recent years, deep neural networks have also been trained to predict range information based on monocular [3], [4] or stereo images [5], [6]. Evidential top-view grid maps enable modeling free space, traffic participants and information on their semantics in a common representation. It is desired to combine measurements from heterogeneous sensors to cope with erroneous measurements by resolving

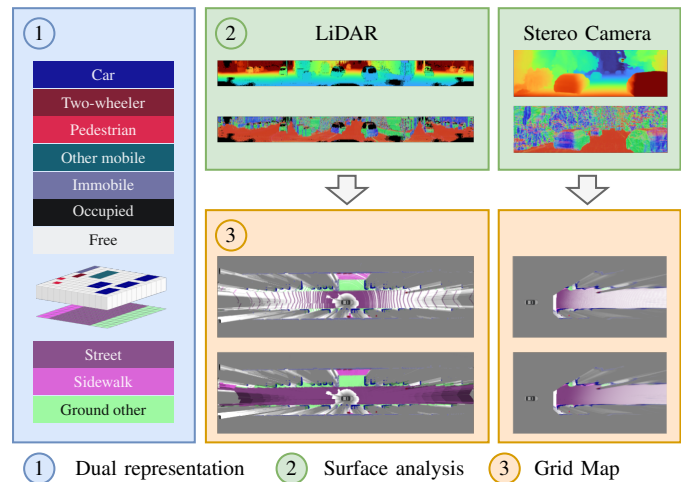


Fig. 1. The proposed evidential grid mapping framework for input data given as images. Range images from LiDAR or disparity images from stereo cameras are transformed into a surface normal vector image. This enables the deduction of occupancy evidence for detections on blocking surfaces. The evidential grid map is estimated using two sensor models where semantic estimates for the ground and for occupancy may optionally be included.

measurement conflicts. One way to facilitate evidential data fusion is to estimate grid maps based on measurements from different sensor sources and combine them on a grid map level.

In this work, we propose a new method to estimate evidential top-view grid maps with measurements from imaging sensors, see Figure 1. We present a novel dual representation that separates the environment into two layers in Section III. The semantic state of the ground is estimated in the first layer and cell occupancy is modeled in the second layer. Therefore, we propose two formal definitions of the term “occupancy” as a basis of our estimation. Then, we present a generic framework to estimate evidence masses for this evidential model in Section IV. This framework is first specified for measurements represented as point sets and subsequently discussed in detail for measurements given as images. By utilizing the organized structure of images, surface normal vectors can be calculated efficiently and occupancy evidence can be deduced for blocking surfaces. For modelling spatial uncertainty, two sensor models are proposed that are calculated on sensor-dependent measurement grids such as Polar grids for LiDARs and u/disparity grids for stereo cameras. In Section V, we present experiments with sensor measurements from a LiDAR

<sup>1</sup> Authors are with the Institute of Measurement and Control Systems, Karlsruhe Institute of Technology (KIT), Karlsruhe, Germany. {sven.richter, frank.bieder, stiller}@kit.edu

<sup>2</sup> Authors are with the Mobile Perception Systems Group, FZI Research Center for Information Technology, Karlsruhe, Germany.

<sup>3</sup> Author is with the Bosch Center for Artificial Intelligence, Renningen, Germany. sascha.wirges@de.bosch.com

\* Corresponding author.

and a stereo camera in the publicly available SemanticKitti dataset [7]. Besides showing qualitative results, we provide a detailed comparison study to demonstrate the robustness of our approach in challenging traffic scenarios.

### A. Evidence Theory

In Evidence Theory [8], the basic belief assignment (BBA)

$$m: \mathcal{P}(\Omega) \rightarrow [0, 1], \quad m(\emptyset) = 0, \quad \sum_{A \in \mathcal{P}(\Omega)} m(A) = 1 \quad (1)$$

assigns a degree of evidence to all possible combinations of hypotheses  $\omega \subseteq \Omega$  contained in the powerset  $\mathcal{P}(\Omega)$ . The hypotheses set  $\Omega$  is called frame of discernment (FOD) and consists of mutually excluding hypotheses of interest.

### B. Grid Maps

The two-dimensional (2D) grid  $\mathcal{G} = \mathcal{P}_1 \times \mathcal{P}_2$  on the rectangular region of interest  $\mathcal{R} = I_1 \times I_2 \subset \mathbb{R}^2$ , where

$$\begin{aligned} \mathcal{P}_i &= \{I_{i,k}, k \in \{0, \dots, s_i - 1\}\}, \\ I_{i,k} &= [o_i + k \delta_i, o_i + (k + 1) \delta_i), \quad i \in \{1, 2\} \end{aligned}$$

forms a partition of the interval  $I_i$  with equidistant length  $\delta_i \in \mathbb{R}$ , origin  $o_i \in \mathbb{R}$  and size  $s_i \in \mathbb{N}$ . Hence, each grid cell  $C \in \mathcal{G}$  is a rectangle with side lengths  $(\delta_1, \delta_2)$ .

Grid mapping is the task of estimating a state  $x$  in the state space  $X$  for each grid cell  $C \in \mathcal{G}$ . Therefore, a grid map  $g$  is a mapping

$$g: \mathcal{G} \rightarrow X \quad (2)$$

assigning to each grid cell  $C \in \mathcal{G}$  an element in the state space  $x \in X$ . The state space  $X$  may encode any formalizable information on the local environment.

### C. Inverse Sensor Models

When modeling a sensor measurement  $m$  in a grid cell  $C \in \mathcal{G}$ , spatial uncertainty is modeled by the inverse sensor model given by the conditional probability

$$\Pr(x \in C | x_m), \quad (3)$$

where  $x_m$  is the measured position projected to the top-view grid and  $x$  is the random variable representing the real position. In the remainder of this thesis, we write  $\Pr(C|m)$  for short. While the final representation is usually defined on a Cartesian grid, the inverse sensor model may be calculated in different coordinate systems such as Polar, u/distance or u/disparity grids. The choice of the coordinate system depends on the sensor modalities and is made so that the grid can be aligned with the sensor measurement rays.

## II. RELATED WORK

### A. Grid Mapping with Range Sensors

Elfes [9] proposed to model a range measurement recorded by a Sound Navigation and Ranging (Sonar) sensor by a 2D Gaussian inverse sensor model where the two dimensions correspond to range and angle. Based on the inverse sensor model he derived an occupancy profile that is recursively fused

in a Bayesian framework. Yguel *et al.* [10] applied a simplified one-dimensional inverse sensor model to LiDAR range measurements in a Polar grid. They further focus on formulating the problem of switching coordinates from Polar to Cartesian mathematically and propose a suitable approximation that can be efficiently implemented on the Graphics Processing Unit (GPU). Yu *et al.* [11] handle conflicting measurements by first collecting reflections above a given height threshold in a Polar grid and subsequently transform the measurement counts into a BBA. They treat ground detections as sources of evidence for the hypothesis *free* and apply backward extrapolation to deduce free space evidence to neighboring grid cells. Porębski [12] presented a customizable inverse sensor model to calculate occupancy grid maps. In order to be able to compute accurate probabilities in each grid cell, they proposed a cell selection process and apply either a Gaussian or an exponential distribution to compute the inverse sensor model. Recently, Van Kempen *et al.* [13] proposed an evidential occupancy grid mapping framework using end-to-end learning. They generate synthetic LiDAR point clouds based on simulated scenarios and train a deep neural network that is able to generate BBA layers for the hypotheses *occupied* and *free* successfully modeling uncertainty.

### B. Grid Mapping with Cameras

Badino *et al.* [14] computed an occupancy grid map based on stereo disparity images and used the resulting grid representation to infer free space areas. They compared Gaussian inverse sensor models on a Cartesian, Polar and u/disparity grid, respectively. Yu *et al.* [15] modeled free space in a v/disparity grid and occupancy separately in a u/disparity grid based on stereo measurements and subsequently combine both in an evidential occupancy grid map. Valente *et al.* [16] utilized a ground segmentation in a v/disparity grid and project obstacles in a u/disparity grid. They apply a 2D Gaussian inverse sensor model explicitly modeling errors in the stereo matching. The vast amount of semantic segmentation frameworks in Computer Vision suggests including semantic estimates in Vision-based grid maps. Giovani *et al.* [17] added an occupancy refinement value denoting the semantic state as meta information to their grid map representation. Thomas *et al.* [18] incorporated semantic hypotheses in an evidential framework in order to estimate a geometric road model. Their inverse sensor model considers confidences of the pixelwise semantic segmentation model and pixel location probabilities.

None of the above-mentioned publications models occupancy and semantic estimates in a joint evidential context. In [19]–[21] a sensor grid mapping pipeline was presented estimating a BBA on a FOD containing ground and object hypotheses for range sensors and cameras. Here, we present an advancement of the evidential model and rethink the BBA estimation.

## III. THE EVIDENTIAL GRID MAP MODEL

We define the driving corridor between the ground and the maximal height above ground  $d_{z,\max}$ . This excludes high obstacles such as bridges and tree branches that do not

interfere with the automated vehicle. Let the surface of a traffic scene be implicitly given as  $f_S(x, y, z) = 0$  where  $x, y$  and  $z$  are Cartesian coordinates in the vehicle coordinate system.

**Definition 1.** Let  $f_G: \mathbb{R}^2 \rightarrow \mathbb{R}$  be a function describing an approximation of the ground height and

$$D_C = \{z - f_G(x, y) \mid (x, y) \in C: f_S(x, y, z) = 0\} \quad (4)$$

be the set containing all distances between ground surface and traffic scene surface in grid cell  $C \in \mathcal{G}$ . The grid cell is called *occupied*, if the traffic scene surface intersects with the driving corridor, i.e.

$$\sup(D_C) > 0, \quad \inf(D_C) < d_{z, \max}, \quad (5)$$

where the supremum  $\sup(A)$  is the smallest upper bound and the infimum  $\inf(A)$  is the largest lower bound of an ordered set  $A$ . If both conditions in Equation (5) are not fulfilled the cell is called *free*.

For the condition “ $\sup(D_C) > 0$ ”, the ground surface estimation must be very accurate to exclude all the measurements reflected on the ground. Hence, a small tolerance margin  $\delta_G > 0$  is added in some publications such as [22] so that the condition becomes “ $\sup(D_C) > \delta_G$ ”.

The second definition of the term occupancy is based on the unit normal vector of the surface  $f_S(x, y, z) = 0$ . It can be shown that this normal vector  $n$  is given by the gradient of  $f_S$ :

$$(n_1, n_2, n_3)^T = \frac{\nabla f_S}{|\nabla f_S|}. \quad (6)$$

**Definition 2.** A grid cell  $C \in \mathcal{G}$  is called

- *occupied*, if the angle difference between the surface normal and the z-axis in the vehicle coordinate system exceeds a given threshold  $b_T$ , i.e.

$$\arccos(n_3) > b_T, \quad (7)$$

and the traffic scene surface corresponding to the grid cell is not fully above the driving corridor, i.e.  $\inf(D_C) < d_{z, \max}$ .

- *free*, if the ego vehicle can enter the underlying area in space, i.e. the complete driving corridor is free, or
- *void*, if it is neither free nor occupied.

The cell state *void* is attained in grid cells covered by obstacles where the surface is non-blocking.

In this work, we consider the semantic occupancy hypotheses “car”, “two-wheeler”, “pedestrian”, “other mobile obstacles” or “immobile obstacles” and the ground hypotheses “street”, “sidewalk” and “other ground”. Note that the occupancy hypotheses, e.g. occupied by a car, and the ground hypotheses, e.g. street, are not contradicting. Therefore, we model occupancy and ground state in separate FODs.

Occupancy is estimated within a cuboid whose footprint is given by the grid cell and the height interval  $[0, d_{z, \max}]$  is defined by the driving corridor. In particular, the occupancy FOD

$$\Omega_s := \{c, cy, p, m, nm, f, v\} \quad (8)$$

consists of the hypotheses listed in Table I. Note that this

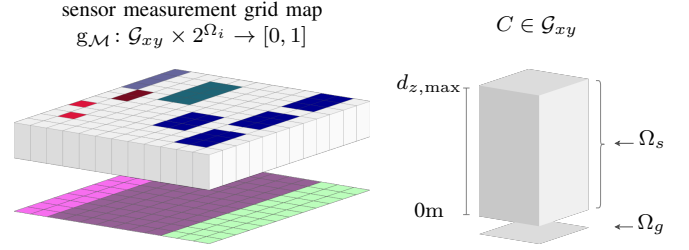


Fig. 2. The evidential grid map model. The dual grid map representation  $g_M$  contains the BBA on the occupancy FOD  $\Omega_s$  and the ground FOD  $\Omega_g$ . Occupancy is estimated in the driving corridor  $[0, d_{z, \max}]$  above ground.

TABLE I  
THE OCCUPANCY FOD.

Semantic class	Set	Letter
Occupied by...		
... car	$\{c\}$	$O_{car}$
... two-wheeler	$\{cy\}$	$O_{tw}$
... pedestrian	$\{p\}$	$O_{ped}$
... other mobile object	$\{om\}$	$O_{om}$
... immobile object	$\{im\}$	$O_{im}$
... unknown object type	$\{c, cy, p, om, im\}$	$O$
Free	$\{f\}$	$F_s$
Neither occupied nor free,	$\{v\}$	$V_s$

FOD can be partitioned as  $\Omega_s \setminus V_s = O \cup F_s$  which is the separation used in classical occupancy grid mapping.

The ground FOD

$$\Omega_g := \{s, sw, t\} \quad (9)$$

describes the semantic state of the ground and consists of the hypotheses listed in Table II.

TABLE II  
THE GROUND FOD.

Semantic class	Set
Street	$\{s\}$
Sidewalk	$\{sw\}$
Other ground	$\{t\}$

The BBA  $m$  on  $\mathcal{P}(\Omega_i), i \in \{s, g\}$  is then represented by the multi-layer grid map

$$g_i: \mathcal{G}_{xy} \times \mathcal{P}(\Omega_i) \rightarrow [0, 1]. \quad (10)$$

The dual evidential representation is sketched in Figure 2. It is based on the assumption that in traffic scenes each obstacle is placed on top of ground implying that every combination of hypotheses  $\theta_1 \in \Omega_s$  and  $\theta_2 \in \Omega_g$  are non contradicting and can thus happen simultaneously. Note that the real world might be composed of several overlapping ground layers as e.g. at freeway exit ramps or bridges. However, even in those scenarios the region of interest can be limited to the ground layer as there is no direct interaction between traffic participants on different ground layers. The simplification of considering one occupancy layer only is justified by the fact that two objects placed on top of each other may be considered as one entity in the navigation module. Therefore, the person sitting on a bicycle is considered as the one entity represented by the hypotheses “occupied by a two-wheeler”.

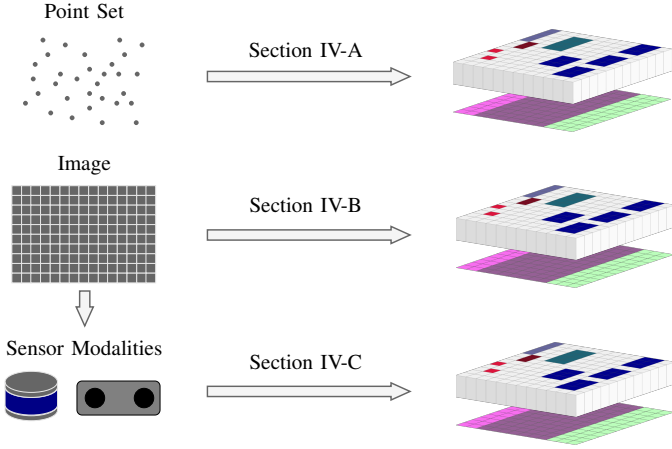


Fig. 3. The methodology described in this section. The evidential grid map estimation is presented for point sets and images. The latter is applied to specific sensors considering their modalities.

#### IV. THE GRID MAPPING FRAMEWORK

Let  $\mathcal{M}$  be a sensor measurement consisting of individual measurement elements  $m \in \mathcal{M}$  with attached semantic label  $\omega_m \in \mathcal{P}(O) \cup \mathcal{P}(\Omega_g)$ . We present a generic framework for transforming the sensor measurement  $\mathcal{M}$  to an evidential grid map  $g_{\mathcal{M}}$ . The outline of the methodology described in this section is sketched in Figure 3.

1) *Occupancy estimation*: Each measurement element  $m$  provides an evidence for occupancy  $\omega \subseteq O$  or ground  $\omega \subseteq \Omega_g$  depending on the attached semantic label  $\omega_m$ . The evidential grid map for hypothesis  $\omega$  in the Cartesian grid cell  $C \in \mathcal{G}_{xy}$  is modeled as

$$g_{\mathcal{M}}(C, \omega) = 1 - \prod_{m \in \mathcal{M}} \Pr(m \nrightarrow \omega, C), \quad (11)$$

where  $\Pr(m \nrightarrow \omega, C)$  is the probability that the measurement element  $m$  is not relevant for hypothesis  $\omega$  in grid cell  $C$ . It is calculated by considering the following four nested binary queries:

- 1) Is the measurement element  $m$  a true positive? The false positive rate  $p_{\text{FP}}$  is a sensor dependent design parameter quantifying the likelihood of obtaining ghost detections.
- 2) Was the measurement element  $m$  recorded on an occupying surface? Methods to calculate the according occupancy probability  $p_{\text{occ}}$  are discussed in Sections IV-A and IV-B.
- 3) Does the semantic label  $\omega_m$  assigned to the measurement element  $m$  match with the considered hypothesis  $\omega$ ? The according probability  $p_{\omega}$  may be obtained from the confidences provided by the pixelwise semantic labeling algorithm. If no such information is available,  $p_{\omega}$  may be set to one if  $\omega_m = \omega$  and zero otherwise.
- 4) Does the measurement element  $m$  provide any evidence for grid cell  $C$  based on its spatial uncertainty? The according probability is given by the inverse sensor model  $\Pr(C|m)$ , presented in Section IV-C.

Consequently, the calculation reads

$$\begin{aligned} \Pr(m \nrightarrow \omega, C) = & p_{\text{FP}} \\ & + (1 - p_{\text{FP}}) \cdot (1 - p_{\text{occ}}) \\ & + (1 - p_{\text{FP}}) \cdot p_{\text{occ}} \cdot (1 - p_{\omega}) \\ & + (1 - p_{\text{FP}}) \cdot p_{\text{occ}} \cdot p_{\omega} \cdot (1 - \Pr(C|m)). \end{aligned} \quad (12)$$

For ground semantics  $\omega \subseteq \Omega_g$  the calculations are done analogously where the second query is negated as ground surfaces are assumed to be non-occupying.

2) *Free space estimation*: A grid cell is free, if no obstacles are present in a defined free space corridor. The free space corridor is limited by the values  $f_{z,\min}, f_{z,\max} \in \mathbb{R}$  denoting the distance to the ground, where  $0 \leq f_{z,\min} < f_{z,\max} \leq d_{z,\max}$ . This relation ensures that the free space corridor is part of the driving corridor. The reason for defining another corridor specifically for the free space estimation is to allow traversing measurement parts of the driving corridor without providing free space evidence. For instance, rays might traverse grid cells below cars. The free space corridor is the height interval where it is very unlikely to have traversing measurements, if the cell is not free. Evidence for the absence of obstacles is provided by measurement rays traversing the grid cell. The free space evidence deduced from each traversing measurement ray is quantified as the ray height relative to the height of the free space corridor. The ray permeability

$$\rho = \frac{d_z}{f_{z,\max} - f_{z,\min}}. \quad (13)$$

is then calculated as the ratio between the height portion  $d_z$  covered by traversing measurement rays and the overall height of the free space corridor. Furthermore, evidence for a cell not being free is obtained by any measurement that provides occupancy evidence. The BBA

$$m(F_s) = \rho \cdot \left( 1 - \sum_{\psi \neq F_s} m(\psi) \right) \quad (14)$$

for free space  $F_s$  is then calculated as the product of the ray permeability  $\rho$  and the part of the BBA mass that has not been assigned to any of the occupancy hypotheses  $\omega \subseteq O$ .

##### A. Grid Mapping with Point Sets

Let the sensor measurement  $\mathcal{M}$  be a point set, i.e. a measurement element  $m \in \mathcal{M}$  is a detection coordinate indicating the presence of a reflecting surface with attached semantic label  $\omega_m$ . Note that other information such as LiDAR intensities or radio detection and ranging (RaDAR) Doppler measurements are omitted here as they are not considered in Equation (12). Point set measurements may be obtained from range sensors such as RaDARs. In point sets, no spatial relation between the elements is given. The calculation of surface normal vectors used in Definition 2 requires finding neighboring elements which is computational expensive. Therefore, occupancy is modeled according to Definition 1 which means that the detection point set is segmented into obstacle and ground detections based on a ground surface model such as

presented in [22]. In Equation (12), the occupancy probability  $p_{occ}$  is then set to one if  $m$  was classified as occupying and to zero otherwise.

The ray permeability  $\rho$  used for the BBA estimation for the hypothesis *free*  $F_s$  is approximated as

$$\rho \approx \frac{h_{\max} - h_{\min}}{f_{z,\max} - f_{z,\min}}, \quad (15)$$

where  $h_{\min}, h_{\max} \in \mathbb{R}$  are the minimal and maximal measured heights of traversing measurement rays within the driving corridor. Note that this approximation may differ from the real ray permeability significantly around obstacles not connected to the ground.

This grid mapping framework for point sets has the disadvantage that a ground surface estimation or an external ground segmentation module is required to estimate the occupancy probability  $p_{occ}$ . This occupies additional computational resources and may introduce errors.

### B. Grid Mapping with Images

In this section, the generic grid mapping pipeline is put into concrete terms for measurements given as images. The measurement images may be provided by different sensor types in different forms such as range images from LiDARs or depth/disparity images from Cameras.

Throughout the processing steps, the representation is transformed to grids defined in different coordinate systems. In particular, the following grids are considered:

a) *Sensor Grid*: The sensor grid  $\mathcal{G}_{uv}$  represents the measurement pattern of the sensor. One sensor reading on  $\mathcal{G}_{uv}$

$$\mathcal{M} = \{f_{\text{range}}: \mathcal{G}_{uv} \rightarrow \mathbb{R} \cup \{\text{unknown}\}, \\ f_{\text{sem}}: \mathcal{G}_{uv} \rightarrow \mathcal{S} \cup \{\text{unknown}\}\},$$

consists of a range measurement given by the mapping  $f_{\text{range}}$  and potentially semantic estimates given by the mapping  $f_{\text{sem}}$ . Here,  $\mathcal{S} = \mathcal{O} \cup \Omega_g$  is the set containing all singleton semantic hypotheses. One sensor element  $m \in \mathcal{M}$  is identified by the 3-tuple  $(C, r_m, \omega_m)$  consisting of the sensor grid cell  $C \in \mathcal{G}_{uv}$ , the range measurement  $r_m \in \mathbb{R}_{>0}$  and the semantic measurement  $\omega_m \in \mathcal{S}$ . The meaning of the range measurement  $r_m$  depends on the sensor and may be the measured distance for LiDAR sensors or the pixel disparity for stereo cameras. Note that the sensor reading  $\mathcal{M}$  marks the entry point of the estimation pipeline presented in this work and that there might be preprocessing steps required to obtain that information from the raw sensor measurements such as disparity calculation or pixelwise semantic labeling.

b) *Measurement Grid*: The measurement grid  $\mathcal{G}_{ur}$  consists of the horizontal sensor grid index  $u$  in the first dimension and discretizes the range measurements interval of interest in the second dimension. When collecting measurements from the sensor grid in the measurement grid, an orthographic projection along the upright Cartesian coordinate axis in the sensor coordinate system is performed. An example for a measurement grid is a grid in Polar coordinates.

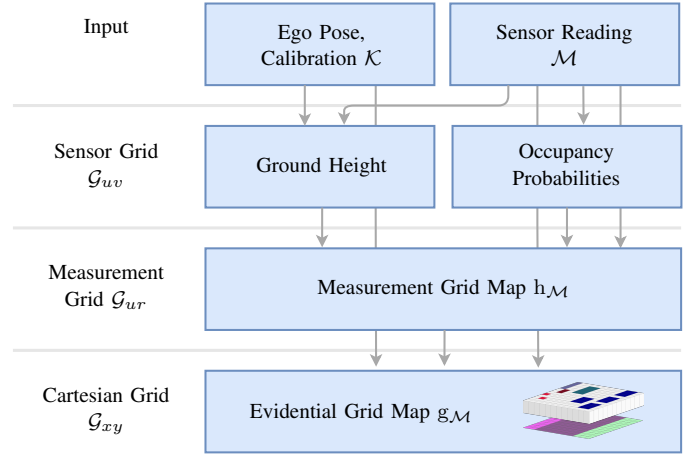


Fig. 4. The processing blocks for calculating the evidential grid map based on input images.

c) *Cartesian Grid*: The final evidential grid map is defined on a Cartesian top-view grid  $\mathcal{G}_{xy}$ . It is defined on a sensor independent coordinate system where the origin is defined with respect to a fixed location on the ego vehicle such as the center of the rear axis.

To indicate the corresponding coordinate system, the considered region of interest is subscripted analogously as  $\mathcal{R}_{uv}$ ,  $\mathcal{R}_{ur}$  and  $\mathcal{R}_{xy}$ , respectively. Furthermore, the mappings

$$\mathcal{T}_{uv}^{ur}: \mathcal{R}_{uv} \rightarrow \mathcal{R}_{ur}, \quad \mathcal{T}_{ur}^{xy}: \mathcal{R}_{ur} \rightarrow \mathcal{R}_{xy}$$

are introduced for transforming coordinates from one system to another.

The individual processing blocks for calculating the evidential grid map  $g_{\mathcal{M}}$  are depicted in Figure 4. The extrinsic and intrinsic sensor calibrations as well as the 6-dimensional ego pose consisting of the 3D position and orientation are assumed to be known. The first processing layer contains image processing steps on the sensor grid  $\mathcal{G}_{uv}$ . First, the surface normal vector is calculated for each measurement element based on the sensor calibration and the input range image. Given the surface normal vectors, the occupancy probability  $p_{occ}$  from Equation (12) can be computed. Subsequently, each pixel is assigned a height above ground by propagating the heights of ground detections along each image column. This information is later used for the free space estimation based on the vertical sensor ray coverage. In the second processing layer a change of coordinates is applied from the sensor grid  $\mathcal{G}_{uv}$  to the top-view measurement grid  $\mathcal{G}_{ur}$ . This coordinate system is chosen according to the sensor characteristics, so that noise can be handled reasonably, and individual rays can be traced efficiently. Here, individual sensor reflections are mapped into the measurement grid map  $h_{\mathcal{M}}$  where evidence for occupancy and free space is accumulated. Finally, the evidential grid map  $g_{\mathcal{M}}$  is calculated based on the measurement grid map  $h_{\mathcal{M}}$  in a common Cartesian grid  $\mathcal{G}_{xy}$ . In the following, we explain the calculation steps on the three grids in detail.

1) *Sensor Grid*: The surface at the reflection locations is analyzed to identify measurement elements that stem from occupying surfaces according to Definition 2. The decision

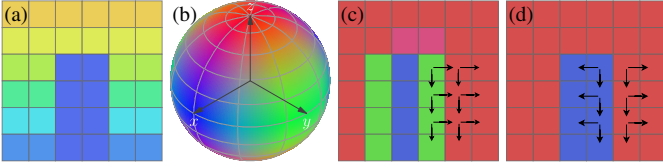


Fig. 5. Pixel-wise surface normal vector calculation based on neighboring pixels: (a) an excerpt of a range image with foreground (blue) and background (yellow-red), (b) the color map on the unit sphere used to visualize surface normal vectors, (c) naive normal vector calculation, (d) normal vector calculation using nearest neighboring pixels.

if a measurement element stems from an occupying surface is made based on the surface normal vector at that location. Instead of providing a binary classification of each measurement element into occupying and non-occupying, we calculate the probability  $p_{occ} \in [0, 1]$  that the surface reflecting the measurement element is occupying. This occupancy probability  $p_{occ}$  can scale the resulting BBA whereas a binary classification results in a loss of information.

Following [23], a bilateral filter is applied to the measurement elements to eliminate noise while preserving edges. Here, the geometric context plays an important role. Averaging applied in the bilateral filter provides desired results if the measurement elements used for calculating the average have similar sources with zero-mean disturbances. In order to increase the likelihood for this, the range image  $f_{range}$  is transformed to images  $f_{height}$  and  $f_{distXY}$  representing the height of the measurement element relative to the sensor origin and the distance to the sensor origin projected to the XY-plane. This selection is based on the assumption that environments in traffic scenes can be separated into sub-planes that are mostly oriented along the XY-plane or perpendicular to it. This holds for the ground surface as well as many objects as buildings and traffic participants. The bilateral filter is then applied to  $f_{height}$  and  $f_{distXY}$  with parameters  $\sigma_{r,height}$  and  $\sigma_{r,distXY}$  denoting the range standard deviation and  $\sigma_{d,height}$  and  $\sigma_{d,distXY}$  denoting the spatial standard deviation.

Based on the filtered images  $\tilde{f}_{height}$  and  $\tilde{f}_{distXY}$ , the surface normal vector can be approximated for each measurement element. Here, the image representation has strong advantages over other representations such as unordered point sets as it implicitly defines a neighborhood. The selection of neighboring pixels used for approximating the surface normal can be crucial. When considering the same neighborhood in each measurement element, the considered values might represent surfaces of different entities and the surface normal calculation will be erroneous, see Figure 5c. To minimize this effect, the considered neighborhood is adapted based on the range measurements. To find the horizontally adjacent pixel  $C_h$ , the next pixel to the left and to the right are considered and the one that has the smaller Euclidean distance in the 3D Cartesian space to the measurement elements is chosen. For the vertically adjacent pixel  $C_v$ , the next pixel below and above are considered. In case no direct neighbors can be found, the second next pixels are considered and so forth until a maximal neighborhood size is reached. This might be necessary in case no reliable measurements were recorded at neighboring

locations. The selection of adjacent pixels used for the normal vector calculation is demonstrated in Figure 5d.

Given the filtered images  $\tilde{f}_{height}$  and  $\tilde{f}_{distXY}$ , the sensor calibration  $\mathcal{K}$  and the pixels  $C, C_h, C_v \in \mathcal{G}_{uv}$ , the Cartesian coordinates  $\vec{p}, \vec{p}_h, \vec{p}_v \in \mathbb{R}^3$  can be calculated and the normal vector  $\vec{n}$  can be determined by computing and normalizing the corresponding cross product

$$\vec{n} = (n_1, n_2, n_3)^T = \frac{(\vec{p}_h - \vec{p}) \times (\vec{p}_v - \vec{p})}{\|(\vec{p}_h - \vec{p}) \times (\vec{p}_v - \vec{p})\|}. \quad (16)$$

Based on the surface normal vector  $\vec{n}$ , an occupancy weight  $w_{occ}$  is calculated. A logistic function centered around  $\frac{\pi}{4}$  is applied to  $\arccos(n_3)$ , i.e. the angle between  $\vec{n}$  and the North Pole  $(0, 0, 1)^T$  as

$$w_{occ} = \frac{1}{1 + \exp(-k(\arccos(n_3) - \frac{\pi}{4}))}, \quad (17)$$

where  $k \in \mathbb{R}_{>0}$  is a scaling factor. The logistic function is parametrized so that we have  $w_{occ} = 0.5$  for  $\arccos(n_3) = \frac{\pi}{4}$  which is based on the geometric consideration that a surface is considered blocking if its slope exceeds  $45^\circ$ .

The credibility of the calculated surface normal vector depends on the distance between the measurement element and its neighbors. If the distance is small it might be dominated by inaccurate range measurements and the resulting normal vector might be disturbed. Therefore, a normal vector confidence value

$$\text{conf}_{\vec{n}} = \frac{1}{1 + \exp(-k'(\min(\|\vec{p}_h - \vec{p}\|, \|\vec{p}_v - \vec{p}\|) - \sigma_{range}))} \quad (18)$$

is calculated quantifying if the minimal distance to the neighboring pixel coordinates is smaller or larger than the standard deviation  $\sigma_{range}$  of the range measurement. Finally, the occupancy probability is calculated as

$$p_{occ} = \text{conf}_{\vec{n}} \cdot w_{occ}. \quad (19)$$

Besides the image  $f_{occ}$  containing the occupancy probabilities, the distance to ground is estimated for each measurement element. This information is needed to exclude measurements outside the considered driving corridor and to clip measurement rays that intersect with the free space corridor boundaries. One option is to explicitly estimate a ground surface using a parametric model such as a plane or a 2D B-spline in the Cartesian space as in [22]. However, estimating a parametric model often comes along with solving an optimization problem with computationally time-consuming numerical solvers. Instead, we estimate the distance to ground directly for each measurement element. Therefore, measurement elements that belong to measurement rays hitting the ground surface are classified, and the measured height is assigned directly. Then the missing regions, i.e. rays that have been reflected by objects, have to be filled. One best guess for this is to traverse the measurement image column-wise and propagate the last known ground height. The height is propagated, if the corresponding measurement element was not reflected on the ground. This classification of a measurement element is done based on the following heuristic considerations:

Let  $C_{uv} \in \mathcal{G}_{uv}$  be the current measurement element. In case  $C_{uv}$  is not located in the bottom row, let  $C_{uv}^{-1} \in \mathcal{G}_{uv}$  be the element located below  $C_{uv}$ . Based on similar geometric considerations as in the calculations of the occupancy weight  $w_{occ}$  (Equation (17)), the measurement element is classified as obstacle, if

- the angle between the surface normal vector  $\vec{n}$  and the North Pole  $(0, 0, 1)^T$  exceeds  $45^\circ$ , i.e.  $\arccos(n_3) > \frac{\pi}{4}$ , or
- $C_{uv}$  is located in the bottom row and the vertical component of the detection coordinate minus the sensor height exceeds a given threshold, or
- $C_{uv}$  is not located in the bottom row and the Euclidean distance in the 3D Cartesian space to the measurement in  $C_{uv} \in \mathcal{G}_{uv}$  is smaller than the distance to the measurement in  $C_{uv}^{-1} \in \mathcal{G}_{uv}$ .

After the first obstacle detection was found in a column, subsequent elements are only classified as ground, if the upper conditions are not fulfilled and the measured height has decreased compared to the measurement in  $C_{uv}^{-1}$ . This is crucial to prevent classifying horizontal surfaces on obstacles as ground.

2) *Measurement Grid*: On the measurement grid  $\mathcal{G}_{ur}$ , measurement elements are assigned to the occupancy hypotheses  $\omega \subseteq \Omega_s$  and ground hypotheses  $\omega \subseteq \Omega_g$  and spatial uncertainty is modeled by applying the inverse sensor model. The multi-layer grid map

$$h_{\mathcal{M}}: \mathcal{G}_{ur} \times (\mathcal{P}(\Omega_g) \cup \mathcal{P}(\Omega_s)) \rightarrow \mathbb{R} \quad (20)$$

accumulates measurement elements for each hypothesis  $\omega \subseteq \Omega_s$  and  $\omega \subseteq \Omega_g$ , respectively, in the corresponding grid layer  $h_{\mathcal{M}}(\cdot, \omega)$ . Based on Equations (11) and (12), the logarithms of the probabilities  $\Pr(m \dashv \omega, C)$  are accumulated as

$$h_{\mathcal{M}}(C, \omega) = \sum_{C_{uv} \in \mathcal{G}_{uv}} \log(\Pr(m \dashv \omega, C)) \quad (21)$$

in grid cell  $C \in \mathcal{G}_{ur}$  for the hypotheses  $\omega \in \mathcal{P}(\Omega_g) \cup \mathcal{P}(\Omega_s) \setminus F_s$ .

For the free space hypothesis  $F_s \subset \Omega_s$ , the ray permeability  $\rho$  defined in Equation (13) is estimated. Therefore, we calculate

$$h_{\mathcal{M}}(C_{ur}, F_s) = \rho_{C_{ur}}. \quad (22)$$

For this purpose, a 3D ray casting is applied based on the sensor intrinsics. The rationale behind this is that the portion of space covered by a measurement ray between the reflecting surface and the sensor origin provides free space evidence. Each measurement ray contributes to the observed height where the contribution is defined by the ray divergence as sketched in Figure 6. For this purpose, we approximately model the vertical ray coverage to be dense, i.e. it is assumed that there are no gaps between the rays. This is justified by the high vertical resolution of the sensors used in this work due to which only insignificant entities may be missed at full ray coverage. Consequently, the ray permeability  $\rho_{C_{ur}}$  in grid cell  $C_{ur} \in \mathcal{G}_{ur}$  is computed as

$$\rho_{C_{ur}} = \frac{d_z}{f_{z,\max} - f_{z,\min}}, \quad d_z = \sum_{C_{uv} \in \mathcal{G}_{uv}} z(r_m), \quad (23)$$

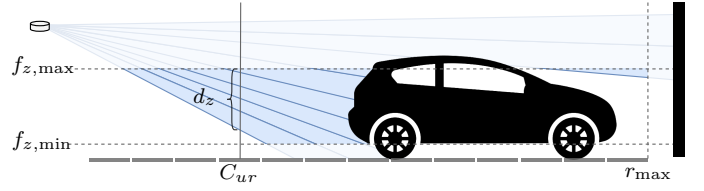


Fig. 6. Calculation of the ray permeability  $\rho_{C_{ur}}$  in a measurement grid cell  $C_{ur} \in \mathcal{G}_{ur}$ . The rays are clipped according to the minimal height  $d_{z,\min}$ , the maximal height  $d_{z,\max}$  and maximal range  $r_{\max}$ .

where  $z$  is a function calculating the height of a measurement ray at range  $r_m$ . Each measurement ray is clipped according to  $f_{z,\min}$ ,  $f_{z,\max}$  as only parts of the ray that traverse the defined free space corridor contribute to the free space estimation. Positive and negative ray heights are mapped into the underlying grid cells to mark end and start points of the clipped measurement rays. The missing gaps can then be filled by simply computing the running sum and correcting the ray heights to account for the ray divergence.

3) *Cartesian Grid*: After calculating the measurement grid map  $h_{\mathcal{M}}$ , the second change of coordinates from the measurement grid  $\mathcal{G}_{ur}$  to the Cartesian grid  $\mathcal{G}_{xy}$  is applied. Therefore, cell values  $h_{\mathcal{M}}(C, \omega)$  must be transformed properly into the Cartesian representation  $h_{xy}(C, \omega)$ . For all hypotheses  $\omega \neq F_s$  except free space, this is done by integrating  $h_{\mathcal{M}}$  over  $\mathcal{T}_{xy}^{ur}(C) \subset \mathcal{R}_{ur}$  as

$$h_{xy}(C, \omega) = \int_{\mathcal{T}_{xy}^{ur}(C)} h_{\mathcal{M}}(x, \omega) dx. \quad (24)$$

For free space  $\omega = F_s$ , the average over  $\mathcal{T}_{xy}^{ur}(C)$  is calculated as

$$h_{xy}(C, F_s) = \frac{1}{\mu(\mathcal{T}_{xy}^{ur}(C))} \int_{\mathcal{T}_{xy}^{ur}(C)} h_{\mathcal{M}}(x, \omega) dx. \quad (25)$$

Here,  $\mu(\cdot)$  denotes the 2D Lebesgue-measure which calculates the area of  $\mathcal{T}_{xy}^{ur}(C)$ .

The Cartesian grid map  $h_{xy}$  is subsequently transformed to a consistent BBA represented by the grid map  $g_{\mathcal{M}}$ . Following Equations (11), (12) and (14), it is computed as

$$g_{\mathcal{M}}(C, \omega) = k(1 - \exp(-h_{xy}(C, \omega))), \quad (26)$$

for  $\omega \subseteq \Omega_s$  or  $\omega \in \Omega_g$ , and

$$g_{\mathcal{M}}(C, F_s) = \left(1 - \sum_{\psi \neq F_s} g_{\mathcal{M}}(C, \psi)\right) h_{xy}(C, \omega) \quad (27)$$

for the free space hypothesis  $F_s \subset \Omega_s$ . Here,

$$k = \frac{1 - \exp\left(-\sum_{\omega \subseteq \Omega_s} h_{\mathcal{M}}(C, \omega)\right)}{\sum_{\omega \subseteq \Omega_s} 1 - \exp(-h_{\mathcal{M}}(C, \omega))} \quad (28)$$

is a normalization factor distributing BBA masses equally to conflicting hypotheses.

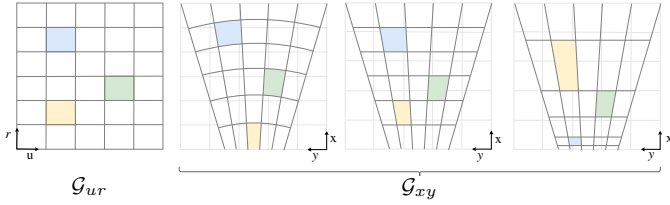
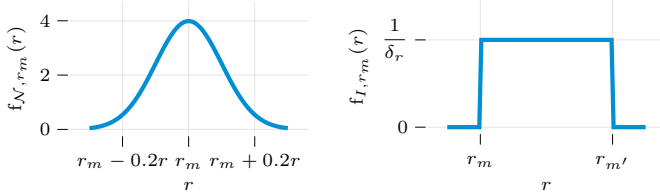


Fig. 7. The measurement grid  $\mathcal{G}_{ur}$  on the left and the transformed Polar, u/distance and u/disparity grid  $\mathcal{T}_{ur}^{xy}(\mathcal{G}_{ur})$ . Matching grid cell colors indicate the same grid cell in the source grid and the warped target grid.



(a) The PDF for the Gaussian inverse sensor model. (b) The PDF for the Interval inverse sensor model.

Fig. 8. The PDFs of the range  $r$  used in the two presented inverse sensor models.

### C. Grid Mapping Considering Sensor Modalities

Up to this point, the inverse sensor model  $\Pr(C|m)$  and the measurement grid  $\mathcal{G}_{ur}$  were not specified as they depend on the sensor modalities. In this section, we present the measurement grids designed for LiDARs, monocular cameras and stereo cameras and two inverse sensor models.

The measurement grid  $\mathcal{G}_{ur}$  used for LiDAR is defined in Polar coordinates, i.e. the horizontal index  $u$  corresponds to the angle location of the spinning laser and the range measurement is the measured distance projected to the  $xy$ -plane. For measurements obtained from a monocular camera where the distance was estimated directly in each pixel, an u/distance grid is used. In case disparity estimates obtained from a stereo camera are mapped, an u/disparity grid is used. Figure 7 shows the relation between the measurement grid  $\mathcal{G}_{ur}$  and the Cartesian grid  $\mathcal{G}_{xy}$  for all three measurement grids used in this work. The cell values in the measurement grid map  $h_{\mathcal{M}}$  are transformed to Cartesian coordinates using Equations (24) and (25).

The inverse sensor model is calculated in the measurement grid  $\mathcal{G}_{ur}$ . Let a measurement grid cell  $C = I_u \times I_r \in \mathcal{G}_{ur}$  be divided into its  $u$  and  $r$  components. We model the measurement  $m$  to be uniformly distributed in  $I_u$ . Hence, the inverse sensor model simplifies to

$$\Pr(C|m) = \Pr(r|r_m) = \int_{r \in I_r} f_{r_m}(r), \quad (29)$$

where  $f_{r_m}$  is the probability density function (PDF) of the range  $r$  given the range measurement  $r_m$ . In this work, we present two options for  $f_{r_m}$ :

a) *The Gaussian Model*: We model the range to be normally distributed with mean  $r_m$  and standard deviation  $\sigma_r$ , i.e.

$$f_{\mathcal{N}, r_m}(r) = \frac{1}{\sqrt{2\pi} \sigma_r} \exp\left(-\frac{1}{2} \left(\frac{r - r_m}{\sigma_r}\right)^2\right). \quad (30)$$

In the remainder of this thesis, we refer to this model as Gaussian inverse sensor model  $\Pr_{\mathcal{N}}(C|m)$ . It is sketched in Figure 8a with standard deviation  $\sigma_r = 0.1r$ .

b) *The Interval Model*: The measurement element  $m$  covers the whole interval  $[r_m, r_{m'}]$ , i.e.

$$f_{I, r_m}(r) = \begin{cases} \frac{1}{\delta_r}, & \text{if } r \in [r_m, r_{m'}] \\ 0, & \text{else,} \end{cases} \quad (31)$$

where  $\delta_r$  is the length of the range interval  $I_r$  of one grid cell  $C \in \mathcal{G}_{ur}$  and  $r_{m'}$  is the range measurement in the sensor grid cell  $C' = (u, v + 1)$  that is vertically adjacent to the considered measurement element  $m$  in  $C$ . Note that  $f_{I, r_m}(r)$  is normalized so that it integrates to one over the range interval  $I_r$  of a fully supported grid cell. This model is based on the assumption that the measurement  $\mathcal{M}$  partitions the measured surface which means that there are no gaps between areas on the world surface covered by rows in the sensor grid  $\mathcal{G}_{uv}$ . In the remainder of this thesis, we refer to this model as Interval inverse sensor model  $\Pr_I(C|m)$ . It is sketched in Figure 8b. We apply  $f_{I, r_m}$  only in the calculation of the BBA on the ground hypotheses  $\Omega_g$  as the model assumption is violated for occupying surfaces. Furthermore, we propose using it only for camera measurements and not for LiDAR measurements as LiDAR scan lines are usually not adjacent. In comparison, the gaps between pixel rows in camera sensor used in automotive applications are negligible.

## V. EXPERIMENTS

Our proposed grid mapping framework is validated using the Kitti Vision Benchmark [24] and the semantic LiDAR point cloud labels from the SemanticKitti dataset extension [7]. They contain measurements from a Velodyne HDL-64E LiDAR scanner with surround view, one RGB and one grayscale stereo camera setup pointing to the front, the sensor calibrations and 6D ego pose annotations. In this work, the measurements from the Velodyne HDL-64E and the stereo RGB camera setup are processed with the presented grid mapping pipeline.

### A. Qualitative Results

In the sensor grid, surface normal vectors are calculated based on the range estimates and occupancy probabilities are deduced as described in Section IV-B1.

Figure 9 shows the image processing steps for a range image of a Velodyne HDL-64E measurement taken from the Kitti dataset. The gaps in the range image result from shadows caused by sensors and antennas on top of the test vehicle or missing reflections due to surfaces with low reflectivity. The latter tends to occur on surfaces at high distances larger than 100m or on dark surfaces such as black cars or windows. The semantically annotated image in the second row contains the labels assigned to each LiDAR detection in the SemanticKitti dataset extension. In the bottom row, the image containing the surface normal vectors colorcoded according to Figure 5b and the resulting image  $f_{\text{occ}}$  containing the occupancy probabilities are shown. Recall that the occupancy probabilities in  $f_{\text{occ}}$  scale with the orientation of the reflecting surface and thus do not



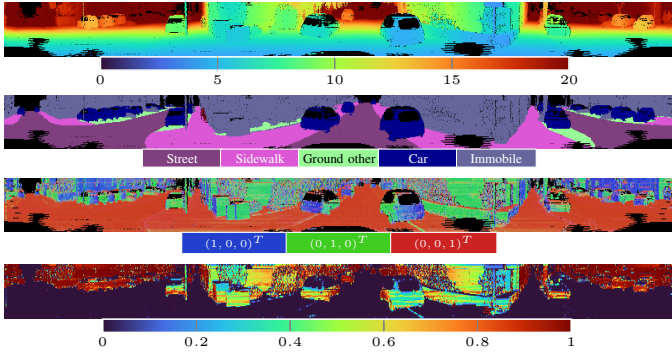


Fig. 9. Impressions of the sensor grid processing chain for a LiDAR sensor reading. From top to bottom: Range image  $f_{\text{range}}$ , semantic segmentation  $f_{\text{sem}}$ , surface normal vectors  $f_{\text{normals}}$  and occupancy probabilities  $f_{\text{occ}}$

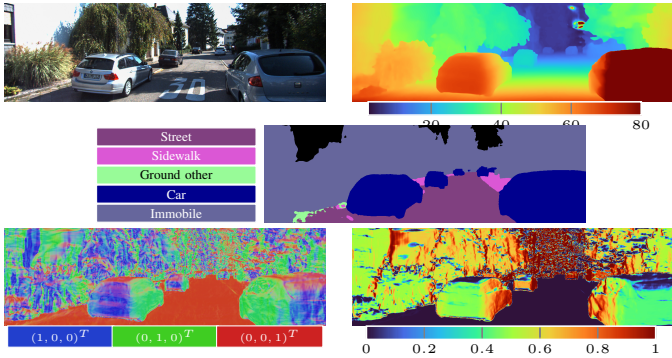


Fig. 10. Impressions of the sensor grid processing chain for a stereo camera sensor reading. From left to right, top to bottom: RGB image, disparity image  $f_{\text{range}}$ , semantic segmentation  $f_{\text{sem}}$ , surface normal vectors  $f_{\text{normals}}$  and occupancy probabilities  $f_{\text{occ}}$

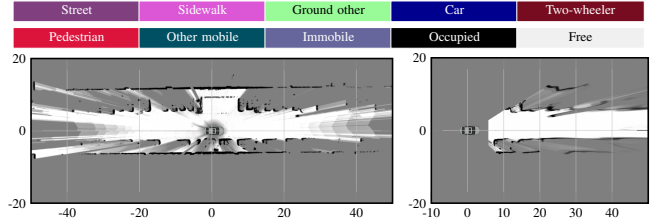
segment the environment in objects and ground. Consequently, there are areas on objects with low occupancy probability on horizontal surfaces such as the hood or the rooftop of cars.

Figure 10 shows the image processing results for an image pair of the stereo camera in the Kitti Tracking dataset. The image view, shows the center part of the LiDAR range image shown in Figure 9. The disparity image depicted on the top right was estimated using the guided aggregation net for stereo matching presented by Zhang *et al.* [5]. This is a well performing stereo disparity estimator generating dense disparity maps that comes along with a real-time capable implementation running at 15-20 frames per seconds (FPS). The pixelwise semantically labelled image in the middle row was obtained by feeding the RGB image recorded by the left camera into the network presented by Zhu *et al.* [25]. The inference on this network is not real-time capable, but similarly performing, real-time capable alternatives have been proposed e.g. in [26]. In the bottom row, the surface normal vectors  $f_{\text{normals}}$  and the corresponding occupancy probability image  $f_{\text{occ}}$  are shown.

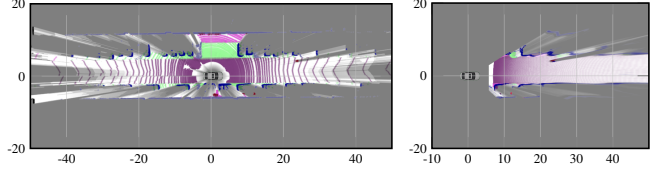
Figure 11 visualizes the resulting grid map estimated with the same measurements as in Figures 9 and 10. First, no semantic estimates are included, i.e. only the 360° LiDAR scan and the stereo disparity map are processed. Figure 11b show the occupancy probability after applying the pignistic



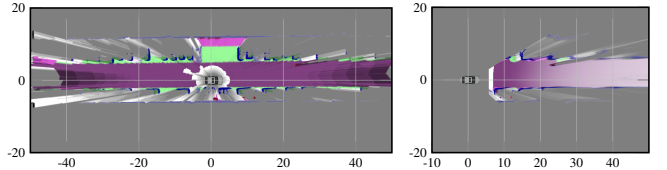
(a) Image taken by the front left color camera.



(b) Resulting grid map without semantic estimates.



(c) Resulting grid map with semantic estimates using the inverse sensor model  $\Pr_{\mathcal{N}}(C|m)$  for both ground and occupancy.



(d) Resulting grid map with semantic estimates using the interval sensor model  $\Pr_{\mathcal{I}}(C|m)$  for occupancy and  $\Pr_{\mathcal{I}}(C|m)$  for the ground.

Fig. 11. Resulting BBA visualizations in the Cartesian grid  $\mathcal{G}_{xy}$  using LiDAR (left) and stereo camera measurements (right) with and without semantic estimates.

transformation

$$\Pr(A) = \sum_{B \subseteq \Omega} \frac{|A \cap B|}{|B|} m(B). \quad (32)$$

Here, the gray values transition from white for zero to black denoting an occupancy probability of one. In Figures 11c and 11d the resulting evidential grid map is visualized when additionally processing the semantic estimates from the pixelwise annotated images. The applied color map shows both ground and object hypotheses and is a combination of the occupancy probability gray value map and a color coding of the semantic classes. The color map was generated based on the following rules: If both a ground hypothesis and an object hypotheses have been assigned a high BBA, the object BBA is visualized. The color saturation scales with the assigned BBA. Above ground, a lower brightness indicates a low BBA for *free*.

The results clearly show the differences in modelling ground detections with the Gaussian inverse sensor model  $\Pr_{\mathcal{N}}(C|m)$  in Figure 11c and with the interval inverse sensor model  $\Pr_{\mathcal{I}}(C|m)$  in Figure 11d. Whereas the BBA estimation for the hypothesis street is sparse using the Gaussian model, evidence for the whole area of the street covered by the sensor grid is obtained when using the interval model.

## B. Occupancy estimation

One of the key tasks in the evidential grid map estimation is the deduction of occupancy evidence based on the measurements. We demonstrate the differences when applying the presented framework to point sets and images. Recall that two ways of defining the term occupied in a geometric manner were presented where Definition 1 is used for point sets and Definition 2 for images. To make the evaluation representable, a subsequence of the Kitti odometry benchmark is chosen that was recorded on challenging terrain with altering height. The BBA for the hypothesis *occupied* is calculated with one of the following three methods:

- *Flat world model.* Derive evidence for occupancy according to Definition 1 as described in Section IV-A. The ground surface is modeled as a xy-plane  $\{(x, y, z) \mid z = 0\}$  in vehicle coordinates and the tolerance margin is set to  $\delta_G = 0.3\text{m}$ . The resulting BBA is denoted as  $m_{\text{flat}}$ .
- *B-spline model.* Derive evidence for occupancy according to Definition 1 as described in Section IV-A. The ground surface is represented by the uniform B-spline model proposed by Wirges *et al.* [22] and the tolerance margin is set to  $\delta_G = 0.3\text{m}$ . The resulting BBA is denoted as  $m_{\text{spline}}$ .
- *Surface normals.* Derive evidence for occupancy according to Definition 2 as described in Section IV-B. The resulting BBA is denoted as  $m_{\text{normals}}$ .

To evaluate the resulting BBA for a cell being occupied the following BBAs are calculated:

- The reference BBA  $m_{\text{ref}}$  calculated using Equation (11) where the occupancy probability is set to

$$p_{\text{occ}} = \begin{cases} 1, & \text{if } \omega_{\text{ref}} \subseteq O, \\ 0, & \text{else,} \end{cases}$$

where  $\omega_{\text{ref}}$  is the semantic label added in the SemanticKitti dataset extension.

- The BBA  $m_{\text{all}}$  containing all detections, i.e. the occupancy weight is  $p_{\text{occ}} = 1$ .
- The three estimated BBAs  $m_{\text{flat}}$ ,  $m_{\text{spline}}$  and  $m_{\text{normals}}$  calculated as described above.

Note that the reference BBA  $m_{\text{ref}}$  is not a ground truth classification based on the same geometric cues as used in the estimation. As opposed to defining occupancy based on geometric constraints as in Definitions 1 and 2, the reference BBA deduces occupancy based on semantic constraints. In order to create a ground truth BBA based on geometric constraints, a complete 3D surface model of the environment would be required. However, the comparison considered here still yields interpretable information on the performance of the BBA estimation. Based on  $m_{\text{ref}}$ ,  $m_{\text{all}}$  and  $m_i$ ,  $i \in \{\text{flat}, \text{spline}, \text{normals}\}$ , the confusion metrics

$$\begin{aligned} \xi_{\text{TP},i} &= \tilde{m}_i(O) \tilde{m}_{\text{ref}}(O) m_{\text{all}}(O), \\ \xi_{\text{FP},i} &= \tilde{m}_i(O) (1 - \tilde{m}_{\text{ref}}(O)) m_{\text{all}}(O), \\ \xi_{\text{FN},i} &= (1 - \tilde{m}_i(O)) \tilde{m}_{\text{ref}}(O) m_{\text{all}}(O), \\ \xi_{\text{TN},i} &= (1 - \tilde{m}_i(O)) (1 - \tilde{m}_{\text{ref}}(O)) m_{\text{all}}(O) \end{aligned}$$

are defined per grid cell  $C \in \mathcal{G}_{xy}$ , where

$$\tilde{m}_i(O) = \frac{m_i(O)}{m_{\text{all}}(O)}, \quad x \in \{\text{flat}, \text{spline}, \text{normals}, \text{ref}\} \quad (33)$$

is the part of  $m_{\text{all}}(O)$  that was classified as occupied. The confusion rates on the whole grid  $\mathcal{G}_{xy}$  are then calculated as

$$\xi_{j,i} = \frac{\sum_{C \in \mathcal{G}_{xy}} \xi_{j,i}(C)}{\sum_{j \in J} \sum_{C \in \mathcal{G}_{xy}} \xi_{\text{TP},i}(C)}, \quad (34)$$

where  $j \in J = \{\text{TP}, \text{FP}, \text{FN}, \text{TN}\}$ . A high false positive rate  $\xi_{\text{FP},i}$  indicates that measurement elements  $m$  with attached semantic label  $\omega_{\text{ref}} \in \Omega_g$  contributed to a high BBA  $m(O)$  whereas a high false negative rate  $\xi_{\text{FN},i}$  indicates that measurement elements with semantic label  $\omega_{\text{ref}} \in O$  had little contribution to  $m(O)$ .

Figure 12 shows the results when processing LiDAR measurements from a Kitti sequence on challenging, hilly terrain. Figure 12a shows a specific frame in that sequence. The ego vehicle enters a street with a significant incline that leads to a crossing on rather flat terrain. The camera image of the front left camera shows that there is a significant change in the gradient of the ground surface in the vicinity of the ego vehicle. This is further highlighted in Figure 12b that shows the maximal detected height of all LiDAR detections located in a grid cell. Here, the LiDAR detections were transformed into the vehicle coordinate system so that zero corresponds to the height below the ego vehicle.

Figure 12c shows the confusion metrics  $\xi_{j,i}$  for 200 consecutive frames in the Kitti sequence. The frame shown in Figures 12a and 12b is marked by the gray vertical line in Figure 12c. The height of the road surface with respect to a global reference coordinate system is visualized in gray behind the plots for the six metrics. Here, all grid cells with assigned ground label *other ground*, i.e. everything but street and sidewalk are excluded as occupancy derived from semantic properties might differ significantly from the geometric occupancy on other ground like meadows and other vegetation. Including those areas would distort the evaluation results. It can be seen that the false positive rate  $\xi_{\text{FP},\text{flat}}$  of the flat world model is heavily influenced by uneven terrain violating the flat world assumption. In most of the frames, the false positive rate  $\xi_{\text{FP},\text{spline}}$  is reduced to approximately zero for the B-spline model. However, between frame 2510 and 2540, a significant rise of  $\xi_{\text{FP},\text{spline}}$  can be observed. The false positive rate  $\xi_{\text{FP},\text{normals}}$  for the proposed surface normal vector-based method, on the other hand, stays almost constant close to zero in the whole test sequence. As in the proposed method, occupancy evidence is not deduced for horizontal surfaces on objects such as car roofs, the false negative rate  $\xi_{\text{FN},\text{normals}}$  is the highest almost throughout the whole sequence. The false negative rate  $\xi_{\text{FN},\text{spline}}$  indicates that the largest number of detections reflected on object surfaces were not missed in the B-spline model. However, it should be emphasized that this is due to the differences between the two underlying occupancy concepts in Definition 1 and Definition 2.

Figure 12d depicts the mapping result when applying grid mapping with point sets using the flat world model. In the area

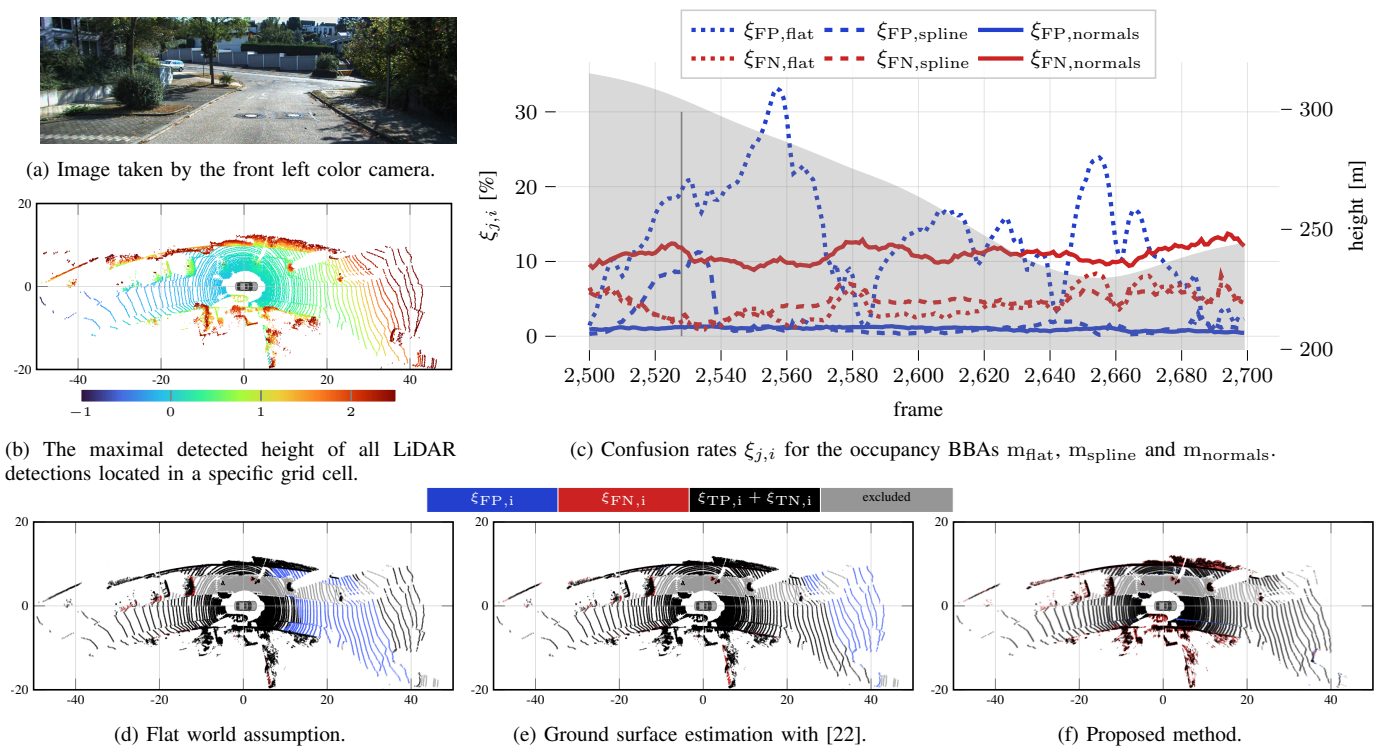


Fig. 12. Evaluation of the occupancy evaluation on challenging, hilly terrain, see (a) and (b). The frame shown in (a), (b), (d), (e) and (f) is marked by the gray vertical line in (c). The comparison in the bottom row demonstrates that our proposed model minimizes false positive occurrences.

around the junction there are many ground detections that are classified as obstacles contributing to a high occupancy mass in those grid cells. On challenging terrain as in this scenario this is expected as the ground model cannot capture the actual ground geometry. Figure 12e shows the results when applying grid mapping with point sets using the B-spline model. The fact that the uniform B-spline is able to capture the real surface significantly better leads to fewer grid cells falsely classified as occupied. However, there are still some grid cells on the ground that are classified as occupied. This can be resolved when applying the proposed surface normal vector model. The results are shown in Figure 12f where a high BBA for the hypothesis occupied is mostly obtained in areas where obstacles are assumed to be present. One exception are curb stones. As opposed to the other two models, the surface normals model classifies grid cells located at curb stones as *occupied*. They are visualized in blue in Figure 12f as curb stones are labeled as sidewalk in the SemanticKitti labels and thus no occupancy evidence is deduced in the calculation of the reference BBA  $m_{ref}$ . The results shown in Figure 12f further show that missing detections in  $m_{normals}$  are in fact almost entirely located within objects and thus are negligible in top-view object shape estimation.

## VI. CONCLUSION

We proposed a novel grid mapping pipeline for LiDAR and camera measurements containing two advancements compared to past publications. First, we base our evidential grid maps on a dual evidential representation modeling semantic occupancy and ground separately. Second, our framework

utilizes a surface orientation-based occupancy evidence deduction making an additional ground surface estimation obsolete. We demonstrated in challenging, hilly traffic scenarios that our method provides detailed and robust mapping results. Our future work will focus on improving sensor data fusion results and combining measurements over time in a recursive estimator. We think that especially the latter will benefit from the dual representation presented in this work.

## REFERENCES

- [1] H. Hirschmuller, "Stereo processing by semiglobal matching and mutual information," *IEEE Transactions on Pattern Analysis and Machine Intelligence*, vol. 30, no. 2, pp. 328–341, 2008.
- [2] M. Bleyer, C. Rhemann, and C. Rother, "Patchmatch stereo - stereo matching with slanted support windows," in *BMVC*, Jan. 2011.
- [3] S. Qiao, Y. Zhu, H. Adam, A. Yuille, and L.-C. Chen, "Vip-deeplab: Learning visual perception with depth-aware video panoptic segmentation," in *Proceedings of the IEEE/CVF Conference on Computer Vision and Pattern Recognition*, 2021, pp. 3997–4008.
- [4] W. Yuan, X. Gu, Z. Dai, S. Zhu, and P. Tan, "New crfs: Neural window fully-connected crfs for monocular depth estimation," *arXiv preprint arXiv:2203.01502*, 2022.
- [5] F. Zhang, V. Prisacariu, R. Yang, and P. H. S. Torr, "Ga-net: Guided aggregation net for end-to-end stereo matching," in *2019 IEEE/CVF Conference on Computer Vision and Pattern Recognition (CVPR)*, 2019, pp. 185–194.
- [6] X. Cheng, Y. Zhong, M. Harandi, Y. Dai, X. Chang, H. Li, *et al.*, "Hierarchical neural architecture search for deep stereo matching," *Advances in Neural Information Processing Systems*, vol. 33, pp. 22 158–22 169, 2020.

- [7] J. Behley, M. Garbade, A. Milioto, J. Quenzel, S. Behnke, C. Stachniss, *et al.*, “SemanticKITTI: A Dataset for Semantic Scene Understanding of LiDAR Sequences,” in *Proc. of the IEEE/CVF International Conf. on Computer Vision (ICCV)*, 2019.
- [8] G. Shafer, “A mathematical theory of evidence,” 1976.
- [9] A. Elfes, “Using occupancy grids for mobile robot perception and navigation,” *Computer*, vol. 22, no. 6, pp. 46–57, 1989.
- [10] M. Yguel, O. Aycard, and C. Laugier, “Efficient gpu-based construction of occupancy grids using several laser range-finders,” vol. 6, pp. 48–83, Jan. 2008.
- [11] C. Yu, V. Cherfaoui, and P. Bonnifait, “An evidential sensor model for velodyne scan grids,” in *2014 13th International Conference on Control Automation Robotics Vision (ICARCV)*, 2014, pp. 583–588.
- [12] J. Porębski, “Customizable inverse sensor model for bayesian and dempster-shafer occupancy grid frameworks,” in *Advanced, Contemporary Control*, A. Bartoszewicz, J. Kabziński, and J. Kacprzyk, Eds., Cham: Springer International Publishing, 2020, pp. 1225–1236, ISBN: 978-3-030-50936-1.
- [13] R. Van Kempen, B. Lampe, T. Woopen, and L. Eckstein, “A simulation-based end-to-end learning framework for evidential occupancy grid mapping,” in *2021 IEEE Intelligent Vehicles Symposium (IV)*, 2021, pp. 934–939.
- [14] H. Badino and U. Franke, “Free Space Computation Using Stochastic Occupancy Grids and Dynamic Programming,” Tech. Rep., 2007, pp. 1–12.
- [15] C. Yu, V. Cherfaoui, and P. Bonnifait, “Evidential occupancy grid mapping with stereo-vision,” in *2015 IEEE Intelligent Vehicles Symposium (IV)*, 2015, pp. 712–717.
- [16] M. Valente, C. Joly, and A. de la Fortelle, “Fusing laser scanner and stereo camera in evidential grid maps,” in *2018 15th International Conference on Control, Automation, Robotics and Vision (ICARCV)*, 2018, pp. 990–997.
- [17] B. V. Giovani, A. C. Victorino, and J. V. Ferreira, “Stereo Vision for Dynamic Urban Environment Perception Using Semantic Context in Evidential Grid,” *IEEE Conference on Intelligent Transportation Systems, Proceedings, ITSC*, vol. 2015-October, pp. 2471–2476, 2015.
- [18] J. Thomas, J. Tatsch, W. van Ekeren, R. Rojas, and A. Knoll, “Semantic grid-based road model estimation for autonomous driving,” in *2019 IEEE Intelligent Vehicles Symposium (IV)*, 2019, pp. 2329–2336.
- [19] S. Richter, S. Wirges, H. Königshof, and C. Stiller, “Fusion of range measurements and semantic estimates in an evidential framework,” *tm - Technisches Messen*, vol. 86, no. s1, pp. 102–106, 2019.
- [20] S. Richter, J. Beck, S. Wirges, and C. Stiller, “Semantic evidential grid mapping based on stereo vision,” in *2020 IEEE International Conference on Multisensor Fusion and Integration for Intelligent Systems (MFI)*, Karlsruhe, Germany, 2020, pp. 179–184.
- [21] S. Richter, Y. Wang, J. Beck, S. Wirges, and C. Stiller, “Semantic evidential grid mapping using monocular and stereo cameras,” *Sensors*, vol. 21, no. 10, 2021, ISSN: 1424-8220.
- [22] S. Wirges, K. Rösch, F. Bieder, and C. Stiller, “Fast and robust ground surface estimation from lidar measurements using uniform b-splines,” in *2021 IEEE 24th International Conference on Information Fusion (FUSION)*, 2021, pp. 1–7.
- [23] R. A. Newcombe, S. Izadi, O. Hilliges, D. Molyneaux, D. Kim, A. J. Davison, *et al.*, “Kinectfusion: Real-time dense surface mapping and tracking,” in *2011 10th IEEE International Symposium on Mixed and Augmented Reality*, 2011, pp. 127–136.
- [24] A. Geiger, P. Lenz, and R. Urtasun, “Are we ready for autonomous driving? the kitti vision benchmark suite,” in *Conference on Computer Vision and Pattern Recognition (CVPR)*, 2012.
- [25] Y. Zhu, K. Sapra, F. A. Reda, K. J. Shih, S. Newsam, A. Tao, *et al.*, “Improving semantic segmentation via video propagation and label relaxation,” in *Proceedings of the IEEE Conference on Computer Vision and Pattern Recognition*, 2019, pp. 8856–8865.
- [26] Y. Hong, H. Pan, W. Sun, and Y. Jia, “Deep dual-resolution networks for real-time and accurate semantic segmentation of road scenes,” *arXiv preprint arXiv:2101.06085*, 2021.